JOURNAL OF COMPUTATIONAL PHYSICS **136,** 115–131 (1997)
ARTICLE NO. CP975748

A Spectral Model for Two-Dimensional Incompressible Fluid Flow in a Circular Basin

II. Numerical Examples

W. T. M. Verkley

Royal Netherlands Meteorological Institute, P.O. Box 201, 3730 AE De Bilt, The Netherlands
E-mail: verkley@knmi.nl

Received February 19, 1997; revised May 14, 1997

In the accompanying paper (Part I; W. T. M. Verkley, 1997, *J. Comput. Phys.* 100–114 **136**) a spectral numerical scheme is developed for two-dimensional incompressible fluid flow in a circular basin. The model is formulated in terms of basis functions that are products of Jacobi polynomials and complex exponentials. The Jacobi polynomials are used for the radial dependence of the fields and the complex exponentials for the angular dependence. The basis functions are orthogonal with respect to the natural inner product for a circular domain. The nonlinear advection term is calculated without aliasing using the transform method, based on a grid of which the radii are Gaussian and the angles are equidistant. In the present paper we discuss the performance of the model by showing examples of time integrations. The differences between these examples concern the spatial structure of the planetary vorticity (γ-plane, β-plane, f-plane), the temporal and spatial resolution of the model, and the form, strength, and type of the forcing and dissipation.

1. INTRODUCTION

In the paper accompanying the present one, which will be referred to as Part I [17], a spectral model is developed for the numerical simulation of two-dimensional and incompressible fluid flow in a circular basin. Such a model is believed to be a useful tool in the study of systems which are two-dimensional to an appropriate first approximation. Examples of such systems are plasmas in a magnetic field and large-scale atmospheric and oceanic flows [5, 10]. Indeed, numerical experimentation is a powerful way of obtaining insight into the behavior of such systems. The evolution of the flow can be studied in as much detail as one likes. Furthermore, numerical simulations can be used to test, e.g., modern statistical mechanical approaches to the long-time behavior of these systems. The present paper is concerned with checking the proposed model against results from other sources in the form of specific examples of time integrations. In the following we give a summary of the model as developed in Part I. An overview of the examples that will be discussed is given in the last paragraph of this Introduction.

The equation that is central to this study and which will be discretized spectrally describes the horizontal advection of the absolute vorticity q by a nondivergent velocity field $\mathbf{v} = \mathbf{k} \times \nabla\psi$, where $\mathbf{k}$ is a vertically pointing unit vector and ψ is a streamfunction. The streamfunction is assumed to be zero at the circular boundary, implying no-normal flow at the boundary. The equation reads:

$$\frac{\partial q}{\partial t} + J(\psi, q) + \tau\phi + \kappa\zeta = 0, \tag{1}$$

where the absolute vorticity q is given by $\zeta + f$, with the relative vorticity ζ being $\mathbf{k} \cdot \nabla \times \mathbf{v} = \nabla^2\psi$ and f being the planetary vorticity. The operators ∇^2 and J are the Laplace and Jacobi operators, respectively, the expressions of which are given in Subsection 2.2 of Part I. The system is forced by a source of vorticity $-\tau\phi$ and damped by Ekman friction $-\kappa\zeta$. Here ϕ is the spatial structure of the forcing (taken to be constant in space and time) and τ and κ measure the strength of the forcing and the friction. Besides Ekman friction, in some cases a viscosity term $\nu\nabla^2\zeta$ is used on the right-hand side of (1). In the latter case we impose as an extra boundary condition that the radial derivative of ψ is equal to the velocity u_b of the boundary, implying no-slip at the boundary.

The functions that are used to discretize the spatial structure of the fields are denoted by $Y_{mn}(r, \theta)$, where m is an integer that runs from $-\infty$ to ∞ and n is an integer assuming the values $|m|$, $|m| + 2$, $|m| + 4$, etc., and where the arguments r and θ are polar coordinates. These polar coordinates are used alongside the Cartesian coordinates x and y, to which they are related by $x = r \cos\theta$ and $y = r \sin\theta$. The flow domain is a circle with radius 1, lengths being expressed in units of the actual radius R, and is sketched in Fig. 1 of Part I. The basis functions are defined by

$$Y_{mn}(r, \theta) \equiv W_{mn}(r)e^{im\theta}, \tag{2}$$

where

$$W_{mn}(r) \equiv r^{|m|}P_k^{(0,|m|)}(s), \tag{3}$$

0021-9991/97 $25.00

and $P_k^{(\alpha,\beta)}(s)$ is a Jacobi polynomial with argument $s = 2r^2 - 1$ and degree $2k$ with $k = (n - |m|)/2$. (see Abramowitz and Stegun [1, Chap. 22]). The functions Y_{mn} can be conveniently represented by means of a diagram like Fig. 2 in Part I. Each dot in this figure signifies a particular basis function. A few examples of the functions W_{mn} in the definition of Y_{mn} are given in Table I of Part I. The basis functions are orthogonal with respect to the natural inner product (see (6) of Part I) for a circular domain. It is instructive to note that the basis functions Y_{mn} span the same linear function space as the functions X_{mn}, which are defined by

$$X_{mn}(r, \theta) \equiv V_{mn}(r)e^{im\theta}, \tag{4}$$

where

$$V_{mn}(r) \equiv r^{|m|}r^{2k} = r^n. \tag{5}$$

We see that the r dependence of both Y_{mn} and X_{mn} is a polynomial of degree n. The functions can be transformed into each other by the formulas given in Appendix A of Part I. In addition, it can be verified that the functions X_{mn} span the same space as the functions $1, x, y, x^2, xy, y^2, x^3, x^2y, xy^2, y^3$, etc. The fact that the functions Y_{mn} and X_{mn} span the same function space as products of polynomials of x and y explains that n increases in steps of 2. Furthermore, because polynomials in x and y form a complete set in terms of which any square integrable function of x and y on a bounded domain can be represented, the sets of functions X_{mn} and Y_{mn} are complete too.

In the spectral model, fields with the dimension of vorticity—like q and ζ—are assumed to be elements of the space *TN*. By this we mean that these fields, collectively denoted by η and distinguished from the original untruncated fields by a hat, are written as

$$\hat{\eta} = \sum_{m=-N}^{N} \sum_{n=|m|}^{N} \eta_{mn} Y_{mn}, \tag{6}$$

where it is understood that the summation over n goes in steps of 2. In Part I it is shown that fields with the dimension of the streamfunction—like ψ—which are obtained by applying the inverse Laplace operator on vorticity fields are elements of the space *UN*. By this we mean that these fields, collectively denoted by χ and distinguished from the original untruncated fields by a tilde, are written as (with the same step convention with regard to the summation over n as in (6))

$$\tilde{\chi} = \sum_{m=-N}^{N} \sum_{n=|m|}^{N+2} \chi_{mn} Y_{mn}. \tag{7}$$

For fields in the space *UN* the summation over n extends to $N + 2$ instead of N. In Subsection 2.2 of Part I expressions are given for the Laplacian and its inverse in terms of the basis functions Y_{mn}. It is also shown there how the spectral coefficients J_{mn} of the Jacobian of a streamfunction and a vorticity field, truncated to the space *TN*, can be calculated without aliasing. The spectral model is then formulated as

$$\frac{\partial \hat{q}}{\partial t} + \mathscr{P}_N J(\tilde{\psi}, \hat{q}) + \tau\hat{\phi} + \kappa\hat{\zeta} = 0, \tag{8}$$

where $\mathscr{P}_N$ is defined to be the operator that projects on the space *TN*. Written out in terms of coefficients this equation reads

$$\frac{dq_{mn}}{dt} + J_{mn} + \tau\phi_{mn} + \kappa\zeta_{mn} = 0, \tag{9}$$

where the coefficients of q_{mn} and ζ_{mn} are related by $q_{mn} = \zeta_{mn} + f_{mn}$ and those of ζ_{mn} and ψ_{mn} by Eq. (17) of Part I. Expressions of the coefficients J_{mn} are given in (20) of Part I. A fourth-order Runge–Kutta scheme, also discussed in Part I, is used to step the system forward in time.

Important global quantities of the system are the absolute enstrophy, circulation, angular momentum, and energy. Using that $\mathbf{v} = \mathbf{k} \times \nabla\psi$ and employing partial integration in the integration over r, these quantities can be written in terms of the inner product (6) of Part I

$$Q_N = \frac{\pi}{2}\langle \hat{q}, \hat{q} \rangle, \tag{10}$$

$$C_N = \pi\langle 1, \hat{\zeta} \rangle, \tag{11}$$

$$A_N = -2\pi\langle \tilde{\psi}, 1 \rangle, \tag{12}$$

$$E_N = -\frac{\pi}{2}\langle \tilde{\psi}, \hat{\zeta} \rangle. \tag{13}$$

In the inviscid case, i.e., the case without forcing and friction, the equations without space and time discretizations conserve absolute enstrophy, circulation as well as energy, and, if the planetary vorticity is circularly symmetric, also angular momentum. In Part I it is shown that, without forcing and friction, the absolute enstrophy and the circulation are still conserved in the semidiscrete system, i.e., in the system with spatial discretization but without the Runge–Kutta time discretization. Also the angular momentum remains conserved, under the condition that the planetary vorticity is circularly symmetric. The energy is not conserved. However, in the first two examples of the next section we will see that if the spatial resolution in-

creases the degree of conservation of energy increases as well and at a rapid pace.

If a viscosity term is added to our system, so that the right-hand side of (1) is $\nu\nabla^2\zeta$, an extra boundary condition of no-slip needs to be imposed. If the boundary moves with a prescribed velocity $u_b(\theta)$, this additional boundary condition can be written as

$$\left[\frac{\partial\tilde{\psi}(r,\theta)}{\partial r}\right]_{r=1} = u_b(\theta). \tag{14}$$

As the streamfunction is completely determined from the vorticity by (16b) or (17b) of Part I, any additional boundary condition must be incorporated in terms of a constraint on the vorticity. If the boundary velocity is written as a finite sum of complex exponentials

$$u_b(\theta) = \sum_{m=-N}^{N} u_{bm} e^{im\theta}, \tag{15}$$

it is shown in Part I that the boundary condition (14) reduces to

$$\zeta_{m|m|} = 2(|m| + 1)\, u_{bm}. \tag{16}$$

So, the no-slip boundary condition fixes the coefficients $\zeta_{m|m|}$ in terms of the Fourier coefficients u_{bm} of the velocity of the boundary. How this condition on the coefficients $\zeta_{m|m|}$ can be maintained during a time integration is explained in Subsection 2.4 of Part I.

The next section contains six examples of time integrations. In the first and second example the planetary vorticity is circularly symmetric; i.e., $f = -\gamma r^2$, where r is the radial coordinate. Results are shown of time integrations, without forcing and friction, using two different spatial resolutions and starting from a dipole that rotates with a known angular velocity. This time-dependent solution can be projected analytically on the basis functions of the spectral model, as demonstrated in the Appendix. In the third and fourth examples the planetary vorticity varies linearly with the north–south coordinate y; i.e., $f = \beta y$. This is the system studied by Verkley and Zimmerman [15], referred to as VZ. In one case we start with the state of rest and let the system evolve with values of τ and κ for which the steady state solution is known from VZ. In another case we repeat the experiment with values of τ and κ for which the result is not known. In the fifth and sixth examples the planetary vorticity is taken to be zero; i.e., $f = 0$. The forcing and Ekman friction are also zero but instead the system has a viscosity term and is driven by a moving boundary. We first study the case of a boundary that rotates with angular velocity ω_b, a fraction σ of which is stationary due to a fixed sleeve. We then consider a boundary that moves with a velocity given by $\omega_b(1 - \sin\theta)$. Batchelor [2] has shown that—in the limit of vanishing viscosity—the vorticity in the interior gets homogenized at a value that is determined by the velocity of the boundary. Wood [16] has given a general expression for this value of the vorticity in case the streamfunction consists of a single cell, which is the case in the two examples. Applied to the first example the expected value of the vorticity is $2(1 - \sigma)^{1/2}\omega_b$. Applied to the second example the expected value is $2(3/2)^{1/2}\omega_b$. These predictions are checked against long time integrations using low values of the viscosity. Section 3 closes the paper with a summary.

2. EXAMPLES OF TIME INTEGRATIONS

In this section we discuss six examples of time integrations with the model developed in Part I and summarized in the previous section. The model is written in FORTRAN, using double precision (16 bits), and implemented on a Silicon Graphics Indy Workstation. The architecture of the code is copied from a spectral code for two-dimensional incompressible flow on a (hemi)sphere, a code that the author has developed previously following the review of Machenhauer [7].

The examples to be discussed in the following differ, among other aspects, in the spatial structure of the planetary vorticity f. The expression for the planetary vorticity, or Coriolis parameter, reads for a rotating spherical earth

$$f = 2\Omega \sin\phi, \tag{17}$$

where Ω is the angular velocity of the earth's rotation and ϕ is latitude in the geographical spherical coordinate system. (The coordinates in this system are the longitude λ and the latitude ϕ, the latter not to be confused with the spatial structure of the vorticity forcing in (1).) Introducing a rotated spherical coordinate system of which the equator passes through a given point $(0, \phi_0)$ and of which the π meridian coincides with the 0 meridian of the original system, the expression for the planetary vorticity reads

$$f = 2\Omega(\cos\phi_0 \sin\phi' - \sin\phi_0 \cos\lambda' \cos\phi'), \tag{18}$$

where (λ', ϕ') are the coordinates in the rotated coordinate system. If we introduce the local Cartesian coordinates

$$x = (a/R)(\lambda' - \pi), \tag{19a}$$

$$y = (a/R)\phi', \tag{19b}$$

where a is the radius of the earth and R is the radius of the circular basin centered at $(0, \phi_0)$, we obtain, after expanding expression (18) to second order in R/a,

$$f \approx f_0 + \beta y - \gamma r^2, \tag{20}$$

where we have defined

$$f_0 \equiv 2\Omega \sin \phi_0, \tag{21a}$$

$$\beta \equiv 2\Omega(R/a) \cos \phi_0, \tag{21b}$$

$$\gamma \equiv \Omega(R/a)^2 \sin \phi_0, \tag{21c}$$

and where $r^2 = x^2 + y^2$. For more details—especially concerning the expansion of some differential operators—we refer to Verkley [14]. We see that, if only the zero-order contribution is retained, the planetary vorticity has the constant value f_0 which is called an f-plane. Here we note that, because a constant contribution to the potential vorticity in (1) is dynamically insignificant, the value of f_0 can be taken as zero. Retaining also the first-order contribution to f we obtain what is commonly called a β-plane. This approximation of the planetary vorticity was first used by Rossby [13] in his study of planetary waves in the atmosphere. Including also the second-order contribution to f and placing the center of the basin on the north pole so that the β-term is zero leads to what has been called a γ-plane by Nof [8].

2.1. *The γ-Plane*

The planetary vorticity in this subsection is assumed to vary quadratically with r, i.e., $f(r, \theta) = -\gamma r^2$, called a γ-plane. By measuring time in units of $(\gamma R^2)^{-1}$ the value 1 can be substituted for γ, so that the planetary vorticity becomes

$$f(r, \theta) = -r^2. \tag{22}$$

We will show that if τ and κ are both equal to zero, the following streamfunction and absolute vorticity are an exact time-dependent solution of (1),

$$\psi(r, \theta, t) = A(r^2 - 1) + BJ_l(\alpha r) \cos l(\theta - \omega t - \mu), \tag{23}$$

$$q(r, \theta, t) = 4A - r^2 - \alpha^2 BJ_l(\alpha r) \cos l(\theta - \omega t - \mu), \tag{24}$$

with

$$\omega = 2\left(A - \frac{1}{\alpha^2}\right). \tag{25}$$

Here $J_l(\alpha r)$ is a Bessel function with integer order l and radial wave number α. The value of the latter is chosen such that $J_l(\alpha) = 0$ as a result of which ψ is zero at the boundary. The product of $J_l(\alpha r)$ and a trigonometric function with angular wavenumber l is an eigenfunction of the Laplace operator with eigenvalue $-\alpha^2$; as a result (24) is indeed the absolute vorticity associated with the streamfunction (23). The parameter B is an arbitrary amplitude and the parameter μ is an arbitrary phase.

Expression (24) is indeed an exact time-dependent solution of (1) and rotates with angular velocity ω given by (25). This follows from the fact that for an absolute vorticity field of the form (24) we have

$$\frac{\partial q}{\partial t} = -\omega \frac{\partial q}{\partial \theta} = J\left(-\frac{1}{2}\omega r^2, q\right), \tag{26}$$

so that

$$\frac{\partial q}{\partial t} + J(\psi, q) = J\left(\psi - \frac{1}{2}\omega r^2, q\right). \tag{27}$$

The last Jacobian is zero because, as can be verified from (23), (24), and (25), there is a linear functional relationship between $\psi - 1/2\omega r^2$ and q,

$$q = A(4 - \alpha^2) - \alpha^2 (\psi - \tfrac{1}{2}\omega r^2). \tag{28}$$

We choose $l = 1$ and the smallest value of α for which $J_1(\alpha) = 0$, which is $\alpha = 3.8316....$ This gives a dipole structure for the streamfunction and the absolute vorticity. The value of α was obtained by searching for the first nontrivial zero of $J_1(\alpha)$, using an interval halving method.[1] Bessel functions, here and in the following are calculated using the numerical routines of Press *et al.* [11]. For the parameter A we choose the value that gives a negative angular velocity ω with a corresponding period of 50 nondimensional time units, i.e., $\omega = -0.1256....$ It follows from (25) that the value of A is $0.005279....$ For the parameter B we take the value 0.1 and for μ the value $\pi/2$.

We initialized the model with the q-field (24) at time $t = 0$. As the model is formulated in terms of coefficients with respect to the basis functions Y_{mn}, we need to project this initial q-field on the functions Y_{mn}. This projection can be done exactly. Indeed, from Table I of Part I it follows that the θ-independent terms can be expressed simply in terms of $Y_{0,0}(r, \theta) = 1$ and $Y_{0,2}(r, \theta) = 2r^2 - 1$. In the Appendix it is proved furthermore that we have

$$J_l(\alpha r) \cos l(\theta - \omega t - \mu) = \sum_{n=l}^{\infty} (c_{ln} Y_{ln}(r, \theta) + c_{ln}^* Y_{-ln}(r, \theta)), \tag{29}$$

with

$$c_{ln} = \frac{1}{\alpha} e^{-il(\omega t + \mu)} (-1)^k (n + 1) J_{n+1}(\alpha), \tag{30}$$

[1] We did our own numerical calculation to make sure that it is an accurate zero of our approximated Bessel function. In fact, it differs somewhat from the value given by Abramowitz and Stegun [1], which is 3.8317....

where the reader is reminded of the fact that $n = l + 2k$, with $k = 0, 1, 2, ...$, etc. As announced at the beginning of this section, we will use two different truncations for the absolute vorticity q. These truncations are $T5$ and $T10$; these are the maximally allowed truncations for 16 and 32 equidistant θ-values and 8 and 16 Gaussian values of r in the numerical evaluation of the Jacobian, as explained in Subsection 2.2 of Part I. In both cases the time stepping is done with the Runge–Kutta scheme, described in Subsection 2.3 of Part I, with a time step of 0.01 time unit.

The truncated fields $\tilde{\psi}$ and $\hat{q}$ at time $t = 0$ and with truncation $T5$ are shown in Figs. 1a and 1b; the same fields at truncation $T10$ are shown in Figs. 2a and 2b. (The fields in $T10$ truncation are visually indistinguishable from the exact fields.) For each of the two truncations we performed a time integration for a period of 500 time units. After this period the dipolar structure should have rotated 10 times and be returned to its original position. In Figs. 1c and 1d we show $\tilde{\psi}$ and $\hat{q}$ after the integration period for the $T5$ integration; in Figs. 2c and 2d the corresponding fields for the $T10$ integration are shown. The figures show that after the $T5$ integration the dipole has rotated somewhat too fast but has preserved its spatial structure very accurately. In the $T10$ truncation the orientation of the dipole after 500 time units is visually indistinguishable from its original orientation. To be more specific, the difference between the fields before and after the integration are shown in Figs. 1e and 1f ($T5$ integration) and in Figs. 2e and 2f ($T10$ integration). Maxima and minima are denoted by H and L, respectively, and are given in the legends to the figures. In the $T5$ integration the difference field has a weak dipolar structure in both the streamfunction (Fig. 1e) and the vorticity (Fig. 1f). The difference between the maximum and minimum value is about 10% of the difference between the maximum and minimum value of the original fields. In the $T10$ integration the difference fields (Figs. 2e and 2f) also have a dipolar structure but with somewhat more noise superimposed. Here the difference between the maximum and minimum value of the streamfunction difference field is about 0.04% of the difference between the maximum and minimum value of the original streamfunction; for the absolute vorticity difference field this is about 0.08%. In Fig. 3 we give the spectral distribution of the enstrophy (10) of the difference fields. The upper panels (Figs. 3a and 3b) refer to the $T5$ truncation, and the lower panels (Figs. 3c and 3d) refer to the $T10$ truncation. In the left panels we show the natural logarithm of $Q_N^{|m|}$ as a function of $|m|$, where $Q_N^{|m|}$ is the contribution to Q_N of all basis functions with index $+m$ and $-m$. In the right panels we show the natural logarithm of Q_N^n where Q_N^n is the contribution to Q_N of all basis functions with index n. We notice that in all four cases the spectrum is relatively flat. This is also the case for the difference fields in a $T21$ integration, not shown, where the difference between the maximum and minimum values is about 0.005 and 0.05%, respectively, of the difference between the maximum and minimum values of the original streamfunction and absolute vorticity fields.

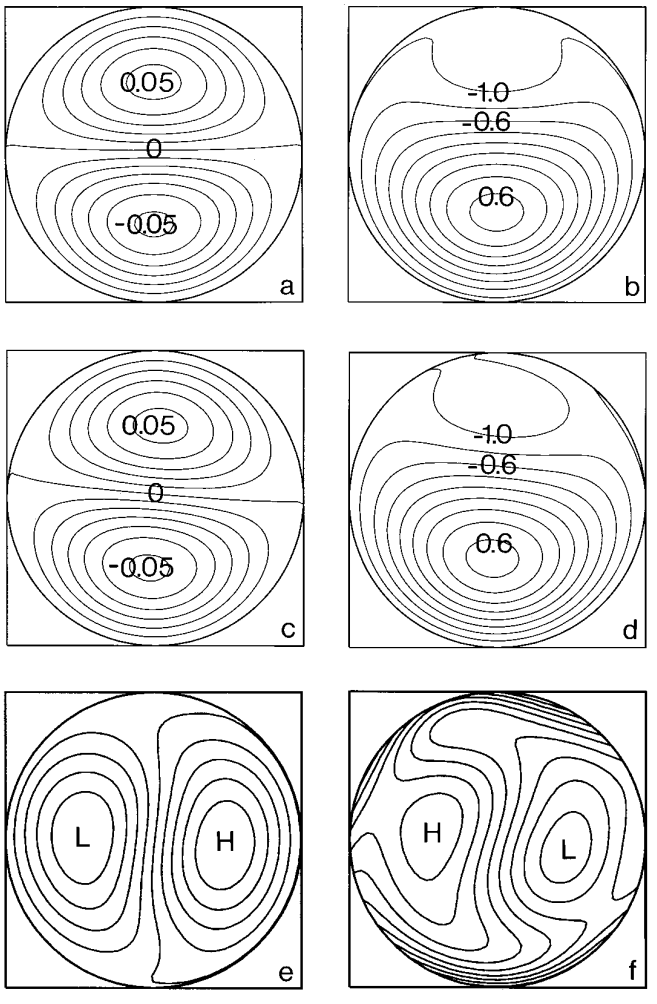

FIG. 1. The truncated streamfunction $\tilde{\psi}$ (a) and absolute vorticity $\hat{q}$ (b) of the exact solution (23) and (24) at $t = 0$, as represented in UN and TN, respectively, with $N = 5$. The parameters of this solution, i.e., A, B, l, α, ω, and μ, are given in the text. The projection on the basis functions Y_{mn} of the model is carried out using (29) and (30). In (c) and (d) the streamfunction $\tilde{\psi}$ and absolute vorticity $\hat{q}$, respectively, are shown at $t = 500$. The difference between the initial streamfunction and the final streamfunction is shown in (e), and the difference between the initial absolute vorticity and the final absolute vorticity is shown in (f). The isoline distance of the difference plots is one-eighth of the difference between the maximum and minimum value, where the (local) minima are marked by L and the (local) maxima by H. In (e) the minimum value is -4.84×10^{-3}; the maximum value is 5.03×10^{-3}. In (f) the minimum value is -8.25×10^{-2}, located at the southern boundary of the basin, whereas the maximum value is 9.08×10^{-2}, located at the northern boundary of the basin.

In Fig. 4 we show the fraction $E_N(t)/E_N(0)$, where $E_N(t)$ is the energy at time t and $E_N(0)$ is the energy at the

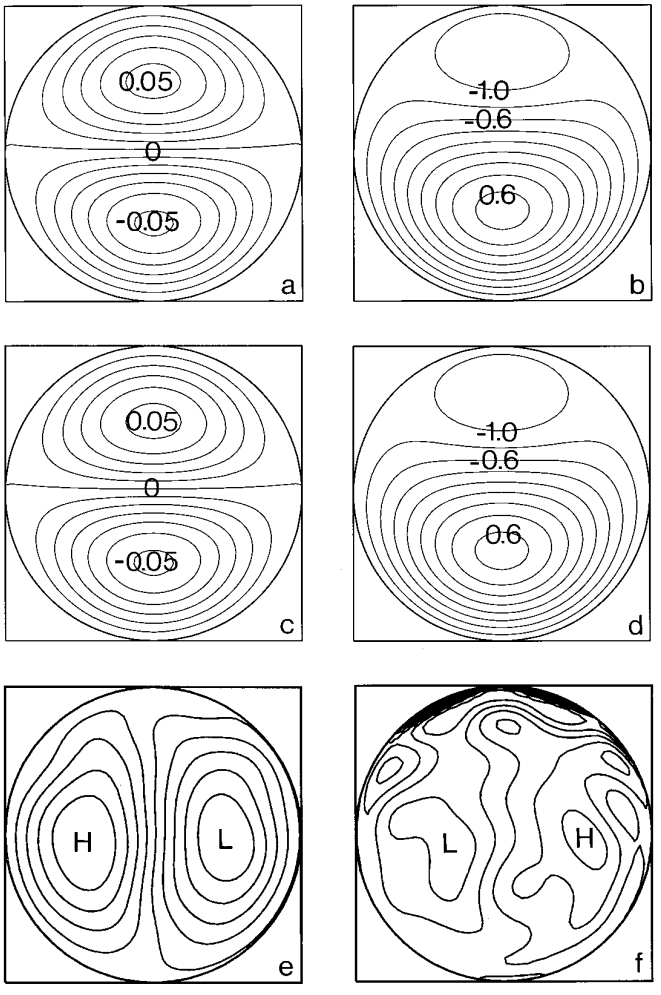

FIG. 2. The truncated streamfunction $\tilde{\psi}$ (a) and absolute vorticity $\hat{q}$ (b) of the exact solution (23) and (24) at $t = 0$, as represented in UN and TN, respectively, with $N = 10$. In (c) and (d) the streamfunction $\tilde{\psi}$ and absolute vorticity $\hat{q}$, respectively, are shown at $t = 500$. The difference between the initial streamfunction and the final streamfunction is shown in (e), and the difference between the initial absolute vorticity and the final absolute vorticity is shown in (f). As in Fig. 1, the isoline distance of the difference plots is one-eighth of the difference between the maximum and minimum value, where the (local) minima are marked by L and the (local) maxima by H. In (e) the minimum value is -2.01×10^{-5}; the maximum value is 1.91×10^{-5}. In (f) the minimum value is -3.67×10^{-4}, whereas the maximum value is 9.68×10^{-4}, located at the northern boundary of the basin.

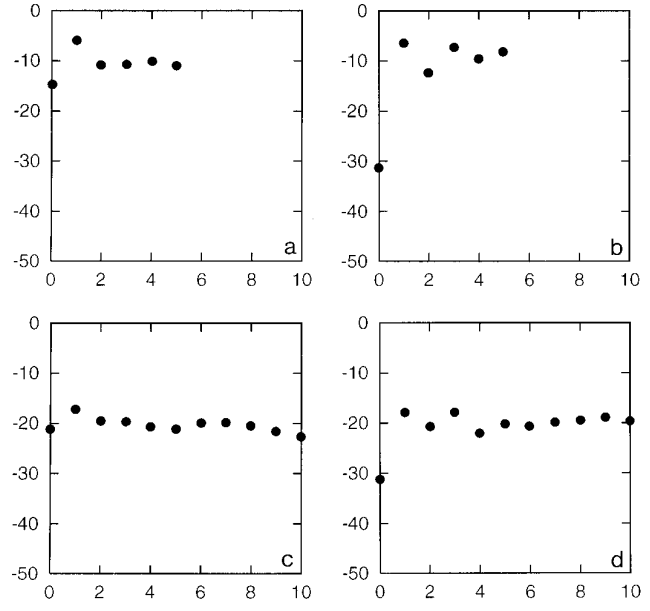

FIG. 3. The spectral distribution of the enstrophy Q_N of the difference between the initial and final state of the time integrations, as displayed in Figs. 1e and 1f and 2e and 2f. In (a) and (b) the natural logarithms of $Q_N^{|m|}$ and Q_N^n are shown as a function of $|m|$ and n, respectively, of the difference between the initial and final state for the $T5$ integration. In (c) and (d) the natural logarithms of $Q_N^{|m|}$ and Q_N^n are shown as a function of $|m|$ and n, respectively, for the $T10$ integration. Here $Q_N^{|m|}$ is defined as the enstrophy contained in the basis functions with index $-m$ and $+m$, and Q_N^n is defined as the enstrophy contained in the basis functions with index n.

start of the integration. Figure 4a is the result of the $T5$ integration, and Fig. 4b is the result of the $T10$ integration. For the case shown in Fig. 4a the variance of the fraction $E_N(t)/E_N(0)$, calculated for 100 points in the time series—5 time units apart—is 1.0×10^{-4}. For the case shown in Fig. 4b this variance is 2.0×10^{-8}. Calculating the same variance for a $T21$ integration, not shown, leads to a value of 1.2×10^{-14}. This, together with the evidence presented in Figs. 4a and 4b, demonstrates clearly that energy conservation improves quickly with increasing resolution, at least in the case of a rotating dipole. We do not show graphs of the fractional changes in the other conserved quantities. In the $T5$ run the variances of the fractions $Q_N(t)/Q_N(0)$, $C_N(t)/$

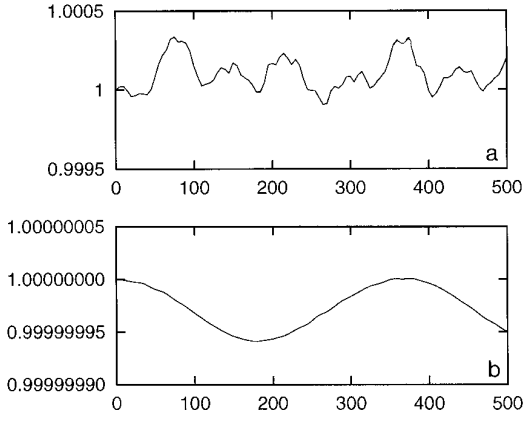

FIG. 4. The value of $E_N(t)/E_N(0)$, where $E_N(t)$ is the energy of the truncated system at time t and $E_N(0)$ is the energy of the truncated system at time 0. The graph in (a) refers to the $T5$ integration, and the graph in (b) to the $T10$ integration.

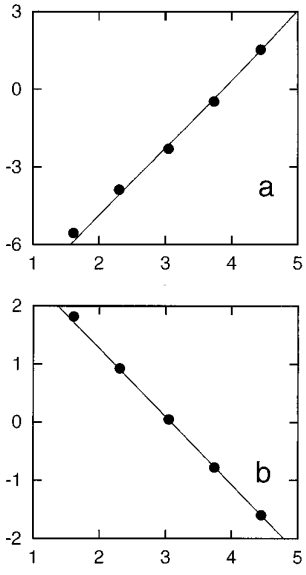

FIG. 5. (a) The natural logarithm of the amount of CPU time (in seconds) required to perform a single time step with the unforced frictionless model as a function of the natural logarithm of the truncation. The five dots correspond to the truncations $N = 5$, 10, 21, 42, and 85. The solid line is proportional to Orszag's [9] estimate for the number of real operations to perform a single time step in a hemispheric spectral model on a sphere. (b) The natural logarithm of the maximum value of the time step as a function of the natural logarithm of the truncation. The maximum value of the time step is determined experimentally using (24) as an initial state. The dots are the five truncations mentioned above. The solid line is the function C/N^p, with $C = 36.37$ and $p = 1.17$. The latter values are determined graphically and provide a reasonable fit to the data.

$C_N(0)$, and $A_N(t)/A_N(0)$ are 8.6×10^{-12}, 5.2×10^{-11}, and 1.1×10^{-10}, respectively. In the $T10$ run the variance of $Q_N(t)/Q_N(0)$ is 4.3×10^{-14}, whereas the variances of $C_N(t)/C_N(0)$ and $A_N(t)/A_N(0)$ are lower than the machine's accuracy, i.e., lower than 1.0×10^{-16}.

As mentioned above, the architecture of the model is copied from a spectral code for incompressible two-dimensional fluid flow on a hemisphere. Indeed, there is an almost perfect one-to-one correspondence between the model developed here and the hemispheric model. The basic difference concerns the functions $W_{mn}(r)$ in the definition of Y_{mn}; in our model they are given by (3), and in the spectral model on a hemisphere they are the associated Legendre functions $P_{mn}(\sin \phi)$ as defined, e.g., by Machenhauer [7]. This one-to-one correspondence implies that we can use Orszag's [9] estimate $(5/4)N^3 + 10N^2 \log_2 N$ for the number of real operations in the calculation of the Jacobian, as a function of the truncation limit N. In Fig. 5a we show the natural logarithm of the CPU time (in seconds) needed for one calculation of the Jacobian as a function of the natural logarithm of the truncation limit. In the calculation we did not use any form of optimization. The five dots in the figure correspond to the truncations $N = 5$, 10, 21, 42, and 85. The solid line in the figure represents Orszag's estimate multiplied by 3.7150×10^{-6} s. The latter time is chosen in order to let the estimate be consistent with the required CPU time per Jacobian for $N = 85$. We conclude that Orszag's estimate provides a reasonable fit to the data and can therefore be used to estimate the CPU time for integrations at higher truncations.

In the integrations shown we used a time step of 0.01 nondimensional time unit. We will see that this is a rather conservative choice. By performing time integrations with increasing values of the time step we can find the maximum value of the time step that does not make the scheme unstable. Instability of our fourth-order Runge–Kutta time-stepping scheme is established by performing 100 time steps, starting with the field (24), and checking whether the enstrophy—which should stay constant—increases by a factor of 1000 or more within the period of 100 time steps. The accuracy of the maximum value of the time step thus obtained is estimated to be 2%. The procedure is carried out for a series of increasing time steps and for the truncations $N = 5$, 10, 21, 42, and 85. The natural logarithm of the maximum time step as a function of the natural logarithm of the truncation limit is shown in Fig. 5b, the dots representing the five different truncations just mentioned. The line in Fig. 5b corresponds to the function C/N^p, with $C = 36.37$ and $p = 1.17$. This function[2] gives a reasonable fit to the points and can be used to estimate the maximum value of the time step at higher truncations.

The maximum value of the time step at truncation $N = 5$ is 6.3 time units; the maximum value of the time step at $N = 10$ is 2.5. At the truncations $N = 21$, 42, and 85 the maximum values of the time step are, respectively, 1.0, 0.45, and 0.20. We recall that these values apply for an integration started with (24) with parameters as given above. The choice of 0.01 as the time step used in the calculations above is indeed well below the maximum value. We have seen that in the first example, with truncation $T5$, the dipole rotates somewhat too fast. This is not due to the value of the time step, as experimentation shows that up to a time step of 1 there is no change in the final position of the dipole after 10 revolutions. With time steps larger than 1, the rotation speed slows down somewhat but in this case the amplitude of the dipole changes somewhat as well.

2.2. *The β-Plane*

In this case the planetary vorticity varies linearly with y, i.e., $f(r, \theta) = \beta r \sin \theta = \beta y$, which is called a β-plane.

[2] A theoretical study of the maximum value of the time step, which is beyond the scope of the present paper, is likely to result in $p = 1$. Use of the latter value would give a somewhat larger estimate of the maximum value of the time step.

If time is measured in units of $(\beta R)^{-1}$, then the planetary vorticity reads

$$f(r, \theta) = r \sin \theta = y. \tag{31}$$

In VZ solutions were obtained for the steady state version of (1) with $f = y$ and $\phi = 1$, i.e., of the equation

$$\kappa\zeta + J(\psi, \zeta + y) + \tau = 0. \tag{32}$$

The essence of the method is a perturbation expansion in which the parameter α,

$$\alpha \equiv \frac{\tau}{2\kappa^2}, \tag{33}$$

is kept fixed and (32) is expanded in either κ^{-1} or δ^{-1}, where the parameter δ is defined by

$$\delta \equiv \frac{\tau}{2\kappa}. \tag{34}$$

The parameter δ measures the ratio between the forcing and friction parameters and thus determines the amplitude of the resulting flow pattern. In the parameter α this amplitude is divided by the friction parameter κ so that α measures the degree of nonlinearity. In VZ both the expansion in κ^{-1} and the expansion in δ^{-1} are used. Here we make use of the expansion in δ^{-1}. It follows from (33) and (34) that in terms of α and δ the original parameters κ and τ can be written as $\kappa = \delta/\alpha$ and $\tau = 2\delta^2/\alpha$. If we substitute the expressions $\kappa = \delta/\alpha$ and $\tau = 2\delta^2/\alpha$ in (32) and divide the equation by δ, we obtain

$$\alpha^{-1}\zeta + \delta^{-1}J(\psi, \zeta + y) + 2\delta\alpha^{-1} = 0. \tag{35}$$

The expansion of ζ and ψ then reads

$$\zeta = \delta\xi_{-1} + \xi_0 + \delta^{-1}\xi_1 + \delta^{-2}\xi_2 + \cdots, \tag{36a}$$

$$\psi = \delta\chi_{-1} + \chi_0 + \delta^{-1}\chi_1 + \delta^{-2}\chi_2 + \cdots. \tag{36b}$$

Substituting these expansions into (35) and collecting like powers of δ^{-1}, we obtain a hierarchy of equations. At order -1 we have

$$\alpha^{-1}\xi_{-1} + J(\chi_{-1}, \xi_{-1}) + 2\alpha^{-1} = 0, \tag{37}$$

which can be solved straightforwardly:

$$\xi_{-1} = -2, \tag{38a}$$

$$\chi_{-1} = -\tfrac{1}{2}(r^2 - 1). \tag{38b}$$

As a result, we have

$$J(\chi_{-1}, \xi) = -\frac{\partial\xi}{\partial\theta}, \tag{39a}$$

$$J(\chi, \xi_{-1}) = 0, \tag{39b}$$

for any field ξ and χ. Using (39), the hierarchy of equations can be written as

$$\xi_{-1} = -2, \tag{40a}$$

$$\left(\alpha^{-1} - \frac{\partial}{\partial\theta}\right)\xi_0 = x, \tag{40b}$$

$$\left(\alpha^{-1} - \frac{\partial}{\partial\theta}\right)\xi_1 = -J(\chi_0, \xi_0 + y), \tag{40c}$$

$$\left(\alpha^{-1} - \frac{\partial}{\partial\theta}\right)\xi_2 = -J(\chi_0, \xi_1) - J(\chi_1, \xi_0 + y), \tag{40d}$$

$$\vdots$$

$$\left(\alpha^{-1} - \frac{\partial}{\partial\theta}\right)\xi_k = -J(\chi_0, \xi_{k-1}) - J(\chi_1, \xi_{k-2}) - \cdots - J(\chi_{k-1}, \xi_0 + y),$$

$$\vdots$$

The equations can be solved consecutively and, as shown in VZ, the solution ξ_k of the kth equation in the hierarchy can be written in terms of the functions X_{mn} with $-k - 1 \le m \le k + 1$ and $|m| \le n \le k + 1$. This means that the solution ξ_k is an element of the space $T(k + 1)$ and the associated streamfunction χ_k an element of $U(k + 1)$. In VZ it is investigated numerically for which values of the parameters the perturbation expansion converges uniformly. In terms of the parameters α and δ the region of uniform convergence is given in Fig. 6. This figure displays the parameters $\ln \alpha$ (on the horizontal axis) and $\ln \delta$ (on the vertical axis). The series converges uniformly outside the shaded region. Figure 6 is identical to Fig. 1 of VZ, except that in Fig. 6 the vertical axis displays $\ln \delta$ instead of $\ln \kappa$. The horizontal line corresponds to the value $\ln \delta = -0.75$ and the three dots D, A, and E are three of the examples discussed in VZ. For these examples the series was summed to $k = 50$ and the corresponding flow patterns are given in Fig. 4 of VZ.

For the purpose of this paper we have repeated the perturbation expansion for point A in the diagram of Fig.

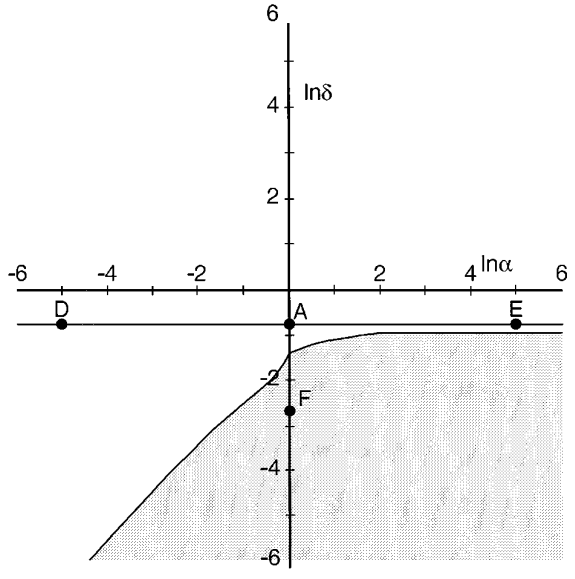

FIG. 6. Convergence diagram of the series expansion method of VZ with ln α on the horizontal axis and ln δ on the vertical axis. The parameter α, defined in (33), is a measure of the nonlinearity of the system, whereas the parameter δ, defined in (34), is a measure of the amplitude of the resulting flow patterns as it measures the ratio of the forcing and friction parameters. Outside the shaded region the series expansion converges uniformly. The points D, A, and E are discussed in VZ. The points A and F correspond to the two time integrations of Subsection 2.2.

6; this point corresponds to ln $\alpha = 0.00$ and ln $\delta = -0.75$ or, equivalently, to ln $\kappa = -0.75$ and ln $\tau = -0.81$. We summed the perturbation series until and including $k = 41$ so that the resulting relative vorticity is an element of the space $T42$. The streamfunction and absolute vorticity of this solution are visually indistinguishable from those of Fig. 4 (second column) of VZ and are not shown here. To check that our time-dependent spectral model is able to find the same steady state by means of a long time integration, we initialized our model with $\tilde{\psi} = 0$ and integrated the model with $f = y$, $\phi = 1$, and κ and τ having the values just given. The truncation used is $T42$, which is the highest possible truncation if 128 equidistant θ-values and 64 Gaussian r-values are used in the numerical calculation of the Jacobian. The period of integration is 50 time units, and the time-stepping procedure is the Runge–Kutta scheme with a time step of 0.01 time unit. The result of this integration is given in Fig. 7. and agrees fully with Fig. 4 (second column) of VZ. We therefore conclude that after 50 time units the system has reached a steady state and that this steady state is in accordance with the result of the series expansion.

As an additional check that after 50 time units the system has reached a steady state we have a look at the time evolution of the absolute enstrophy, circulation, angular momentum, and energy. First we note that the time evolution of the circulation C_N can be calculated analytically. Indeed, we have

$$\frac{dC_N}{dt} = \pi\langle 1, -\tau\hat{\phi} - \kappa\hat{\zeta}\rangle = -\pi\tau\langle 1, 1\rangle - \pi\kappa\langle 1, \hat{\zeta}\rangle \qquad (41)$$

$$= -\pi\tau - \kappa C_N,$$

where we used the fact C_N does not change with time in the absence of forcing and friction, and that $\hat{\phi} = \phi = 1$. The solution of the differential equation is

$$C_N(t) = C_N(0)e^{-\kappa t} + \pi\frac{\tau}{\kappa}(e^{-\kappa t} - 1), \qquad (42)$$

where $C_N(0)$ is the value of C_N at time $t = 0$. It follows from the solution (42) that the value of C_N at $t = \infty$ is given by

$$C_N(\infty) = -\pi\frac{\tau}{\kappa}, \qquad (43)$$

so that (42) can be written as

$$C_N(t) = C_N(0)e^{-\kappa t} + C_N(\infty)(1 - e^{-\kappa t}) \qquad (44)$$

and thus

$$\frac{C_N(t)}{C_N(\infty)} = \frac{C_N(0)}{C_N(\infty)}e^{-\kappa t} + 1 - e^{-\kappa t}. \qquad (45)$$

In our case the value of $C_N(0)$ is 0 so that

$$\frac{C_N(t)}{C_N(\infty)} = 1 - e^{-\kappa t}. \qquad (46)$$

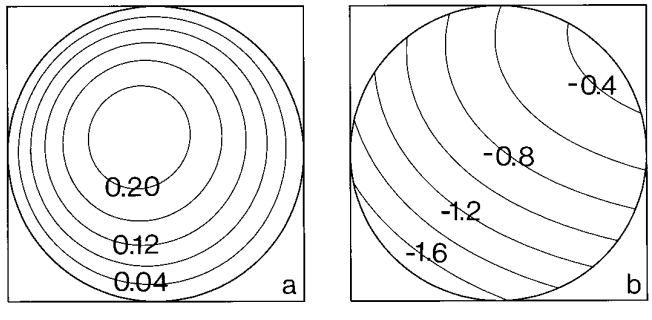

FIG. 7. The streamfunction $\tilde{\psi}$ (left) and the absolute vorticity $\hat{q}$ (right) at time $t = 50$ in the time integration with ln $\alpha = 0$ and ln $\delta = -0.75$. These values correspond to ln $\kappa = -0.75$ and ln $\tau = -0.81$, values for which the series expansion approach of VZ converges (see their Fig. 4, second column). The model resolution is $T42$, the time-stepping fourth-order Runge–Kutta with a time step of 0.01.

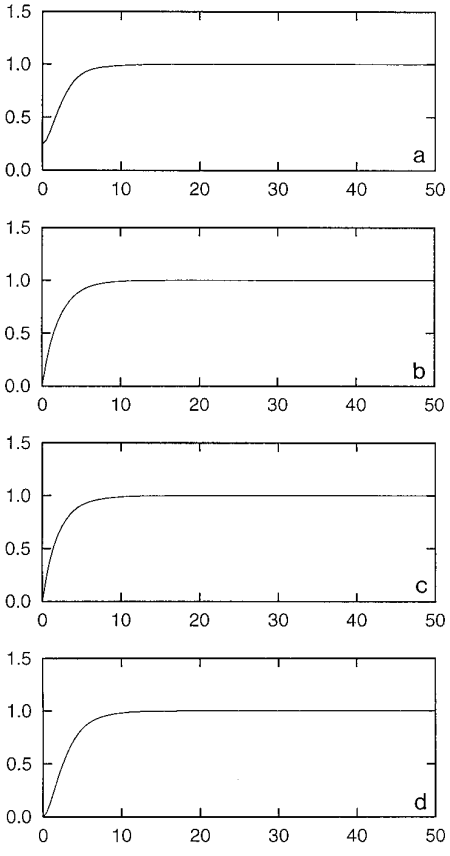

FIG. 8. The fractions $Q_N(t)/Q_N(50)$ (a), $C_N(t)/C_N(50)$ (b), $A_N(t)/A_N(50)$ (c), and $E_N(t)/E_N(50)$ (d) as a function of time. The plots are drawn on the basis of calculated values at times $t = 0.0, 0.5, 1.0, ..., 50.0$, i.e., on the basis of 100 data points. The values at the end of the integration period are $Q_N(50) = 1.61 \times 10^0$, $C_N(50) = -2.79 \times 10^0$, $A_N(50) = -7.09 \times 10^{-1}$, and $E_N(50) = 1.68 \times 10^{-1}$.

After 50 time units the exponential term in the equation above is 5.5×10^{-11} for the value of κ that is chosen here. Assuming that the absolute enstrophy, angular momentum, and energy behave not too differently, it therefore makes sense to substitute the value 50 for ∞ and look at the fractions $Q_N(t)/Q_N(50)$, $C_N(t)/C_N(50)$, $A_N(t)/A_N(50)$, and $E_N(t)/E_N(50)$ of the time integration. The graphs are displayed in Fig. 8. We see that the circulation (Fig. 8b) neatly follows the expected behavior. The other quantities indeed reach their saturation values in about the same way, where we note that the absolute enstrophy (Fig. 8a) starts from a nonzero value due to the contribution of the planetary vorticity f. The values of Q_N, C_N, A_N, and E_N at time $t = 50$ are given in the legend to Fig. 8.

We conclude this subsection by showing the results of a time integration for the parameters $\ln \alpha = 0$ and $\ln \delta = -2.75$ or, equivalently, $\ln \kappa = -2.75$ and $\ln \tau = -4.81$, denoted by point F in Fig. 6. The values of these parameters lie outside the region in which the method of VZ converges, so that this time integration explores unknown territory. Using the same truncation and time stepping as in the previous example we integrate the model for 250 time units, starting from the state of rest. The result is given in Fig. 9. It is a steady state, judged from the fact that the flow patterns at several time values before $t = 250$ cannot be distinguished visually from the pattern of Fig. 9. We observe that this steady state has a much more pronounced boundary layer structure in the north-west part of the basin than the steady state of Fig. 7. The streamfunction has the same general structure as Fig. 5 of Harrison and Stalos [4], who carried out the same type of numerical simulations for a square basin.

That Fig. 9 is a steady state is confirmed by the time evolution of the absolute enstrophy, circulation, angular momentum, and energy, divided by their values at $t = 250$, of which the graphs are given in Fig. 10. We see that all four quantities are close to their saturation values at $t = 250$; these values are given in the legend to Fig. 10. It is observed that also here the circulation $C_N(t)$ neatly follows the expected curve. The exponential term in (46) at $t = 250$ is now 1.2×10^{-7}, which is again considered sufficiently small to identify the values at $t = 250$ with the saturation values.

2.3. *The f-Plane*

In this subsection we take the planetary vorticity to be constant, i.e., $f(r, \theta) = f_0$, which is called an f-plane. If time is measured in units of f_0^{-1}, we may substitute the value 1 for f_0. It should be noted, however, that in the dynamics of (1) a constant value of f has no effect. This means that f is only a measure of time and can effectively taken to be zero. Assuming that the vorticity forcing and the Ekman friction are also zero, and that a viscosity term is present on the right-hand side of (1), the equation to be studied is

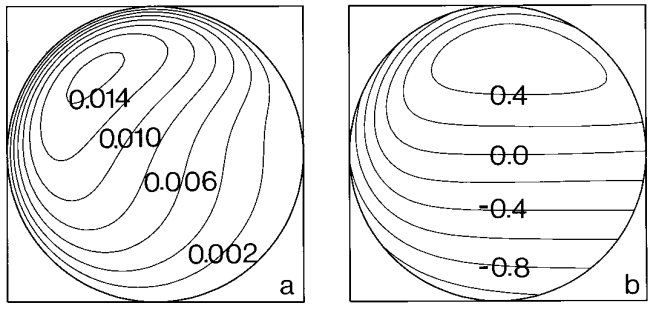

FIG. 9. The streamfunction $\tilde{\psi}$ (left) and the absolute vorticity $\hat{q}$ (right) at time $t = 250$ in the time integration with $\ln \alpha = 0$ and $\ln \delta = -2.75$. These values correspond to $\ln \kappa = -2.75$ and $\ln \tau = -4.81$, values for which the series expansion approach of VZ does not converge. The model resolution is $T42$, the time-stepping fourth–order Runge–Kutta with a time step of 0.01.

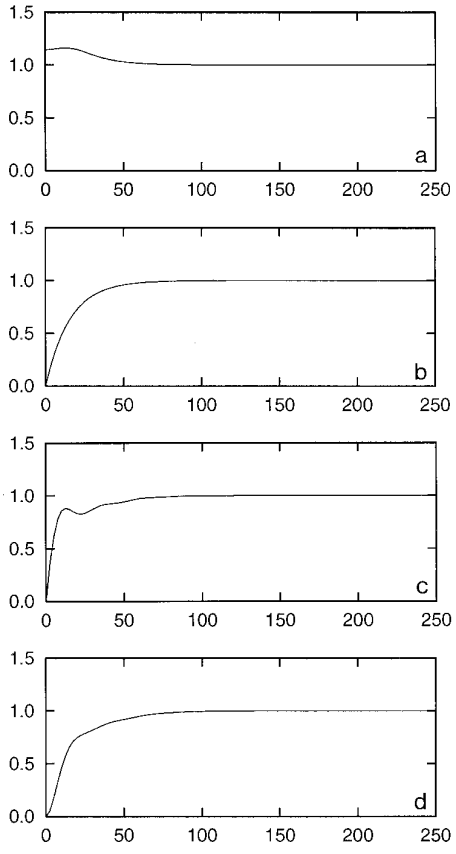

FIG. 10. The fractions $Q_N(t)/Q_N(250)$ (a), $C_N(t)/C_N(250)$ (b), $A_N(t)/A_N(250)$ (c), and $E_N(t)/E_N(250)$ (d) as a function of time. The plots are based on the calculated values at times $t = 0.0, 2.5, 5.0, ..., 250.0$, i.e., on 100 data points. The values at the end of the integration period are $Q_N(250) = 3.43 \times 10^{-1}$, $C_N(250) = -4.02 \times 10^{1}$, $A_N(250) = -4.16 \times 10^{-2}$, and $E_N(250) = 1.33 \times 10^{-3}$.

$$\frac{\partial \zeta}{\partial t} + J(\psi, \zeta) = \nu \nabla^2 \zeta. \tag{47}$$

In this section we will consider steady solutions of this equation. With the Jacobian written as $\mathbf{v} \cdot \nabla \zeta$, it reads

$$\mathbf{v} \cdot \nabla \zeta = \nu \nabla^2 \zeta. \tag{48}$$

We will test our numerical model by performing two long time integrations and analyze the final states that are obtained. We incorporate viscosity and the corresponding no-slip boundary condition in the manner described in Subsection 2.4 of Part I. As a reference we consider the case in which the viscosity is vanishingly small, a case that has been studied theoretically by Batchelor [2]. First, we will give a short outline of his theoretical results, and next we will describe the results of the time integrations.

From the steady state equation (48) it follows that for any region R (not to be confused with the radius of the circular domain) within the flow domain we have

$$\begin{aligned} &\int_R dS \mathbf{v} \cdot \nabla \zeta = \nu \int_R dS \nabla^2 \zeta \Rightarrow \\ &\oint_B dl \mathbf{n} \cdot \mathbf{v} \zeta = \nu \oint_B dl \mathbf{n} \cdot \nabla \zeta, \end{aligned} \tag{49}$$

where dS is an area element of the flow domain, $\mathbf{n}$ is an outward pointing unit vector locally perpendicular to the boundary B of R, and dl is a line element along B. We used that $\mathbf{v} \cdot \nabla \zeta = \nabla \cdot (\mathbf{v}\zeta)$, as $\mathbf{v}$ is divergence free, and applied the divergence theorem. If we now take as a region R a region that is bounded by a closed streamline $\psi = c$, the integral on the left-hand side is zero because $\mathbf{n}$ is then perpendicular to $\mathbf{v}$. We thus obtain

$$\oint_{\psi=c} dl \mathbf{n} \cdot \nabla \zeta = 0. \tag{50}$$

This relationship holds for every flow that is steady in the presence of viscosity. It expresses the fact that in the steady state there can be no diffusive flux of vorticity over regions enclosed by streamlines. In those parts of the flow domain in which the viscosity term in (48) is vanishingly small we have, in addition to (50),

$$\begin{aligned} &\mathbf{v} \cdot \nabla \zeta = 0 \Rightarrow \\ &\zeta = \zeta(\psi); \end{aligned} \tag{51}$$

i.e., the vorticity ζ should be constant on isolines of the streamfunction ψ. Combining (50) with (51), we obtain for those parts of the flow domain in which the viscosity term is vanishingly small

$$\begin{aligned} &\frac{d\zeta}{d\psi} \oint_{\psi=c} dl \mathbf{n} \cdot \nabla \psi = 0 \Rightarrow \\ &\frac{d\zeta}{d\psi} \oint_{\psi=c} dl |\mathbf{v}| = 0 \Rightarrow \\ &\frac{d\zeta}{d\psi} = 0. \end{aligned} \tag{52}$$

As this is true for every closed streamline, the vorticity ζ should have a constant value ζ_0. This is Batchelor's [2] theorem on vorticity homogenization, a theorem that was later elaborated upon by Rhines and Young [12] in the context of planetary gyres.

Although Batchelor's theorem states that the vorticity gets homogenized within closed streamlines the theorem does not say at which value. In order to remove this indeterminacy, the effects of viscosity need to be considered in

more detail. Now, it is well established since the work of Prandtl that viscosity mainly acts in layers adjacent to the flow boundaries. In these boundary layers the viscosity term is not small, not even in the limit of vanishing viscosity as these layers may become vanishingly narrow with correspondingly high values of the velocity gradients. As an example of how an analysis of boundary layers resolves the indeterminacy, Batchelor [2] considered a circular flow domain of which the boundary rotates with constant angular velocity ω_b with a fraction σ that remains stationary due to a fixed sleeve. If this fraction is zero, then it is intuitively clear that the value of ζ_0 should be $2\omega_b$, i.e., the value that corresponds to a solid-body rotation with the same angular velocity as the moving boundary. If this fraction is nonzero, then the solution of the boundary layer problem (which need not be solved in all detail) leads to the result that $\zeta_0 = 2(1 - \sigma)^{1/2}\omega_b$. Wood [16] has shown that for all cases in which the streamfunction consists of a single cell with closed streamlines the value of the homogenized vorticity is given by

$$(\zeta_0/2)^2 = \frac{1}{2\pi}\int_0^{2\pi} d\theta[u_b(\theta)]^2. \tag{53}$$

This expression is Eq. (46) from Kuwahara and Imai [6] and includes Batchelor's result as a special case. Kuwahara and Imai [6] describe, among other results, the result of a numerical procedure for obtaining steady states of the same system as considered here. Their procedure makes use of a relaxation method and finite differences with a grid of equidistant values of r and θ. In one case the resolution of their model was 40×40 and the boundary velocity $\omega_b(1 - \sin\theta)$ with $\omega_b = 0.5$. Wood's formula gives a value of $2(3/2)^{1/2}\omega_b$ for the value of the homogenized vorticity. With a viscosity of 1/1024 Kuwahara and Imai [6] indeed obtained an almost homogenous field of vorticity, as can be judged from their Fig. 3b.

In the following we will describe two time integrations with the model, with a $T42$ spatial truncation (close to the resolution used by Kuwahara and Imai [6]) and a fourth-order Runge–Kutta time-stepping procedure with a time step of 0.01 time unit. In the first time integration we take for the viscosity ν the nondimensional value of 1/1000. This value is large enough to let the model resolve any boundary layers, which are expected to be of the order of $\nu^{1/2}$ (see Batchelor [3, Eqs. (5.7.3) and (5.7.4)], his U_0 and L being of order 1 in our case). As the initial state we choose $\hat{\zeta} = \hat{\zeta}_b$, where $\hat{\zeta}_b$ is the field of which all coefficients are zero except for $\zeta_{m|m|}$ which are given by (16). As explained in the previous section, this initial state satisfies the boundary condition that the tangential velocity at $r = 1$ equals a given field $u_b(\theta)$ of which the complex Fourier coefficients are u_{bm}. In the case discussed by Batchelor [2] the velocity field at the boundary is given by $u_b(\theta) = \omega_b$ for $\theta < \theta_l$ or $\theta > \theta_u$, and $u_b(\theta) = 0$ for $\theta_l \le \theta \le \theta_u$, where $\theta_u - \theta_l = 2\pi\sigma$. The Fourier coefficients u_{bm} of this field can be calculated exactly. However, the truncated field (15) then shows spurious oscillations in the vicinity of θ_l and θ_u as a result of the Gibbs phenomenon. To smooth out these oscillations we approximated the boundary velocity field by

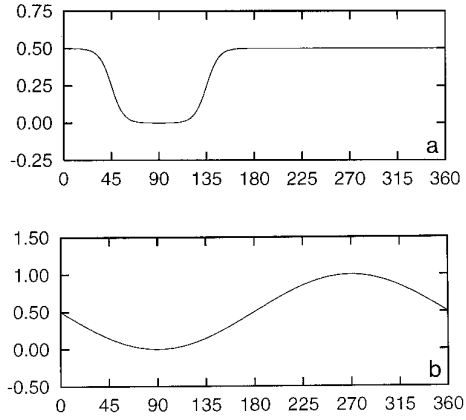

FIG. 11. (a) The velocity field $u_b(\theta)$, given by (54), as represented by (15) with $N = 42$. The velocity field (54) is a smoothed version of the field used by Batchelor [2] in his study on vorticity homogenization. It represents a boundary that rotates with a uniform angular velocity $\omega_b = 0.5$ of which a fraction $\sigma = 1/4$, centered around $\theta = \pi/2$ (90°), is stationary. (b) One of the boundary velocity fields used by Kuwahara and Imai [6], namely $u_b(\theta) = \omega_b(1 - \sin\theta)$, with $\omega_b = 0.5$.

$$u_b(\theta) = \omega_b([1 + e^{\alpha(\theta-\theta_l)}]^{-1} + [1 + e^{\alpha(\theta_u-\theta)}]^{-1}), \tag{54}$$

and calculated the Fourier coefficients numerically by dividing the interval $[0, 2\pi]$ in 1000 equal parts and approximating the Fourier integral by a summation. In the time integration we took $\omega_b = 0.5$, $\alpha = 10$, $\theta_l = \pi/4$ (45°), and $\theta_u = 3\pi/4$ (135°) so that σ equals 1/4. The resulting truncated field $u_b(\theta)$ is in close agreement with (54). A graph of it can be seen in Fig. 11a.

In Figs. 12a and 12b we show the initial streamfunction and vorticity field. The streamfunction describes a large cyclonic (counterclockwise) gyre that fills the whole flow domain. At the northern part of the boundary, at the position of the fixed sleeve, the streamlines are wider apart. The velocities there are weaker than elsewhere and this, of course, agrees with the boundary velocity displayed in Fig. 11a. The vorticity field has its largest gradients at the endpoints of the sleeve, while the gradients in the neighborhood of the southern boundary are more or less constant. Note, incidentally, that the initial vorticity field has a zero Laplacian, so that it is a solution of (48) in the limit of infinitely high viscosity.

For a viscosity as small as 1/1000 the initial state is not stationary and, as soon as the integration starts, vorticity

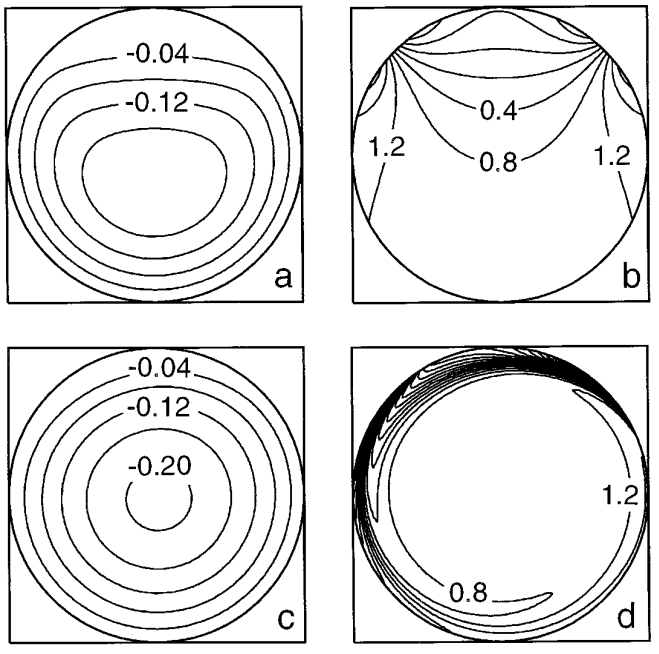

FIG. 12. The streamfunction and the vorticity at time $t = 0$ (a and b, respectively) and at time $t = 500$ (c and d, respectively) in a time integration with the model in $T42$ truncation and a fourth-order Runge–Kutta time-stepping scheme with a time step of 0.01 time unit. The planetary vorticity, vorticity forcing, and Ekman friction are zero, but the system is viscous (with 1/1000 taken for the nondimensional viscosity) and is driven by a boundary that moves with the velocity field u_b displayed in Fig. 11a. Because of the viscosity, the no-slip boundary condition $\partial\psi/\partial r = u_b$ is implemented. The initial state is given by (16) with the other coefficients equal to zero; this field satisfies the no-slip boundary condition and has a zero Laplacian, so that it is in fact a stationary state of the system if the viscosity is infinitely high. The final state shows a considerable amount of homogenization of its vorticity.

from the left endpoint of the sleeve starts moving along the southern boundary in the direction of the flow. In the meantime the vorticity at the left endpoint of the sleeve is reduced, but starts growing again after the vorticity at the southern boundary is partly dissipated. Then the whole process starts again at a lower intensity. This damped periodic behavior has settled down into a nearly steady state after 500 time units. The streamfunction and vorticity at this time are shown in Figs. 12c and 12d. The streamfunction has become more circularly symmetric and its amplitude has increased. The vorticity field has changed markedly. The gradients of the vorticity have concentrated in relatively narrow layers at the boundary. Away from these boundary layers the gradients of the vorticity have been reduced substantially.

We do not show the fractions $Q_N(t)/Q_N(500)$, $C_N(t)/C_N(500)$, $A_N(t)/A_N(500)$, and $E_N(t)/E_N(500)$ but instead remark that all four graphs saturate visually after about 100 time units to a steady value. Within the first 100 time units the fraction $Q_N(t)/Q_N(500)$ undergoes six damped oscillations, whereas $A_N(t)/A_N(500)$ and $E_N(t)/E_N(500)$ asymptote to their saturation values roughly like the corresponding graphs in Fig. 8. We note that the fraction $C_N(t)/C_N(500)$ is and remains 1. This can be understood from the fact that we have from (11)

$$C_N(t) = \pi\langle 1, \hat{\zeta}\rangle = \pi\zeta_{00} \tag{55}$$

and that ζ_{00} is fixed by the boundary condition (16).

A graph of the vorticity along the line $x = 0$ as a function of y is given in Fig. 13a. Here the long-dashed curve corresponds to $t = 0$, the solid curve corresponds to $t = 500$, and the short-dashed horizontal curve denotes the theoretical value $(3/4)^{1/2} = 0.8660....$ Figure 13a quite clearly shows that homogenization of vorticity has taken place and that the gradients have concentrated in relatively narrow boundary layers. At the center of the basin the value of ζ is 0.8607 with an estimated uncertainty of 0.0001. This is very close to the theoretical value. In order to give a more detailed view of the flow close to $r = 1$ we show in Figs. 13b and 13c plots of the streamfunction field (thin lines) and the vorticity field (thick lines) in a rectangular projection in which the horizontal coordinate is θ (in degrees, from 0 to 360) and the vertical coordinate is r (from 1.0 to 0.7). Figure 13b corresponds to the flow at $t = 0$, and Fig. 13c corresponds to the flow at $t = 500$. Figure 13c shows that the boundary layer at $t = 500$ is well behaved, even close to the points where the boundary velocity changes rapidly.

In the second time integration we used one of the boundary velocity profiles discussed by Kuwahara and Imai [6], namely $u_b(\theta) = \omega_b(1 - \sin\theta)$ with $\omega_b = 0.5$. The Fourier coefficients of this field (which is shown in Fig. 11b to compare it with the previous boundary velocity field) are obtained in a straightforward way. The integration is started with $\hat{\zeta} = \hat{\zeta}_b$, where $\hat{\zeta}_b$ is the field of which all coefficients are zero except for $\zeta_{m|m|}$ which are given by (16). Again, this initial state satisfies the boundary condition that the tangential velocity at $r = 1$ equals the given field $u_b(\theta)$ of which the complex Fourier coefficients are u_{bm}. The vorticity field of this initial state field increases linearly with y. In Figs. 14a and 14b we show the initial streamfunction and vorticity field. The streamfunction again describes a large cyclonic (counterclockwise) gyre that fills the whole flow domain. Using the value 1/1024 for the viscosity ν (the value used by Kuwahara and Imai [6]) we let the system evolve in time—using the model described above with $T42$ spatial resolution and a Runge–Kutta time-integration procedure with a time step of 0.01 time unit—for a total period of 500 time units. The streamfunction and vorticity fields after the integration are shown in Figs. 14c and 14d, respectively. A cross section along the line $x = 0$ of the vorticity field at the beginning and the end of the integration along with the constant theoretical value of

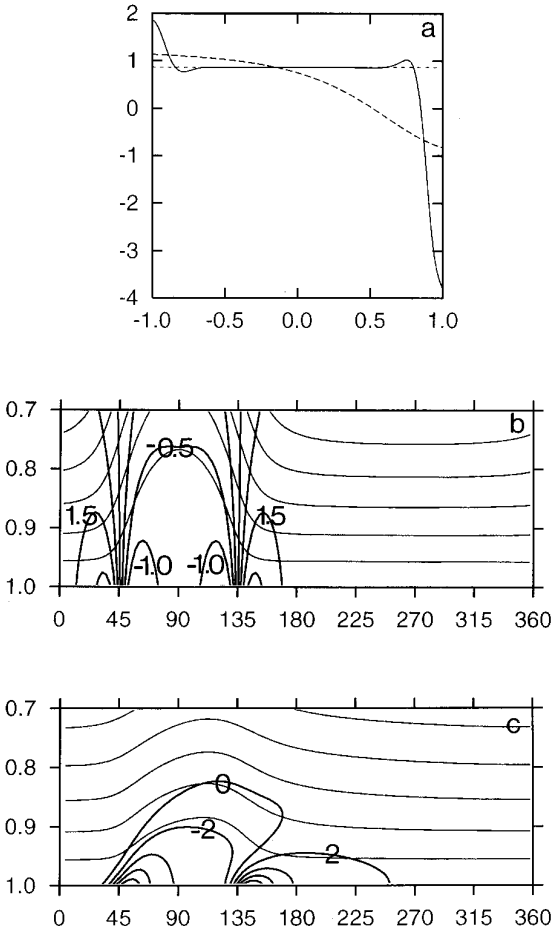

FIG. 13. Cross sections of the vorticity along the line $x = 0$ and isoline plots of the streamfunction and vorticity at time $t = 0$ and time $t = 500$, for the boundary velocity field displayed in Fig. 11a. Panel (a) shows the vorticity along the line $x = 0$ as a function of y; the long-dashed curve corresponds to the initial state, the solid curve to the final state, and the short-dashed curve to the theoretical profile. The figure demonstrates quite clearly that after 500 time units the vorticity in a large part of the interior has become more uniform and that gradients of the vorticity have become concentrated in relatively narrow boundary layers. Panels (b) and (c) show the streamfunction (thin lines) and the vorticity (thick lines) in a projection with θ on the horizontal axis and r on the vertical axis at the initial and final time, respectively. The isolines of the streamfunction are plotted for the values 0.00 (lowest isoline, coinciding with $r = 1$), 0.02, 0.04, etc. The isolines of the vorticity are labeled explicitly, the contour interval being 0.5 in (b) and 2 in (c).

$(3/2)^{1/2} = 1.2247...$ is shown in Fig. 15a. The latter figure is to be compared with Fig. 3b of Kuwahara and Imai [6], which is visually indistinguishable from our Fig. 15a. The value of the vorticity at the center is 1.2669 with an estimated uncertainty of 0.0001. Again, this is close to the theoretical value for vanishing viscosity. A more detailed picture of the flow close to $r = 1$ is shown in Figs. 15b and 15c. As in Fig. 13, these figures show plots of the streamfunction and vorticity field close to $r = 1$ at the initial and final time of the integration.

3. SUMMARY

To study the performance of the spectral model that is developed in the accompanying paper, Part I, we discuss six examples of time integrations. The first two examples are for a γ-plane in which the planetary vorticity f varies quadratically with the radial coordinate r. Here the forcing and friction are set to zero and the system is initialized with a dipolar streamfunction and absolute vorticity of which the time evolution is known exactly. This exact solution, essentially the product of a cosine of θ and a Bessel function of r, can be projected analytically on the basis functions Y_{mn}. The two examples refer to two different truncations, namely $T5$ and $T10$, and are intended to show that the conservation of energy increases rapidly with increasing resolution. Both examples reproduce the uniform rotation of the dipole, although in the $T5$ integration the simulated rate of rotation was visibly too fast. In connection with these two examples we also studied the amount of time required for each time step as well as the maximum value of the time step as a function of the spatial resolution of the model.

The next two examples are for a β-plane where the

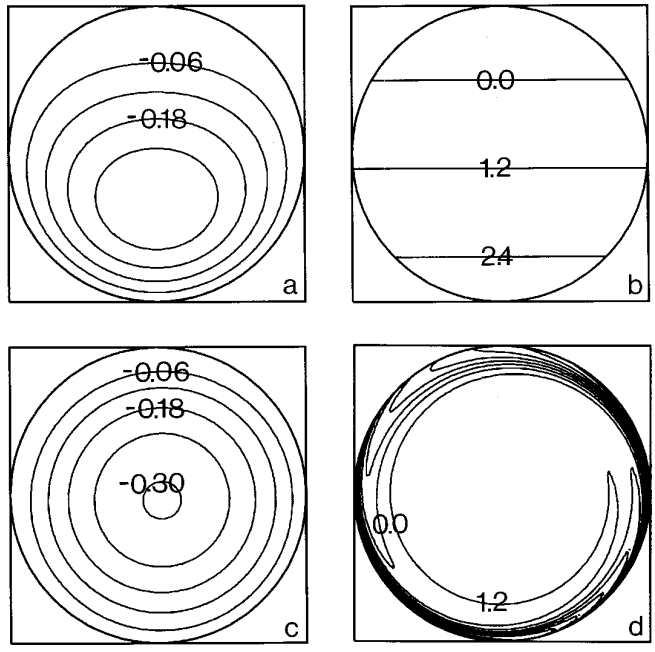

FIG. 14. The streamfunction and the vorticity at time $t = 0$ (a and b, respectively) and at time $t = 500$ (c and d, respectively) in a time integration with the model in $T42$ truncation and a fourth-order Runge–Kutta time-stepping scheme with a time step of 0.01 time unit. As in Fig. 12, the planetary vorticity, vorticity forcing, and Ekman friction are zero, but the system is viscous (with 1/1024 taken for the nondimensional viscosity) and is driven by a boundary that moves with the velocity field u_b displayed in Fig. 11b. The initial state is given by (16) with the other coefficients equal to zero.

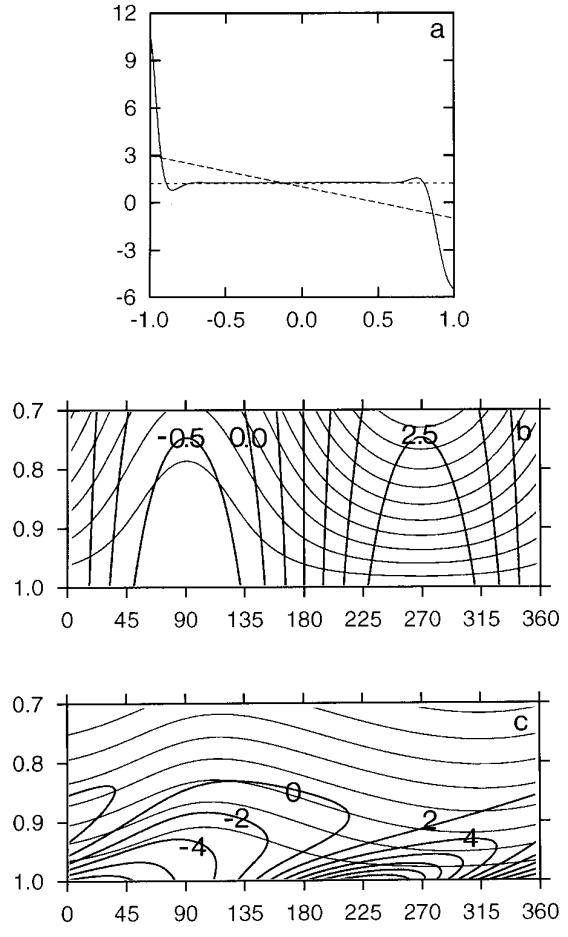

FIG. 15. Cross sections of the vorticity along the line $x = 0$ and isoline plots of the streamfunction and vorticity at time $t = 0$ and time $t = 500$, for the boundary velocity field displayed in Fig. 11b. Panel (a) shows the vorticity along the line $x = 0$ as a function of y; the long-dashed curve corresponds to the initial state, the solid curve to the final state, and the short-dashed curve to the theoretical profile. Panels (b) and (c) show the streamfunction (thin lines) and the vorticity (thick lines) in a projection with θ on the horizontal axis and r on the vertical axis at the initial and final time, respectively. The isolines of the streamfunction are plotted for the values 0.00 (lowest isoline, coinciding with $r = 1$), 0.02, 0.04, etc. The isolines of the vorticity are labeled explicitly, the contour interval being 0.5 in (b) and 2 in (c).

planetary vorticity varies linearly with the north–south coordinate y. The forcing and friction in these examples are of the same form as those used by VZ [15], who developed a perturbation series technique to find steady state solutions of (1). In the first of these examples we performed a time integration for values of the forcing and friction parameters for which the steady state solution is known from VZ. The model, in $T42$ truncation, is integrated long enough to reach a nearly steady state and it is confirmed that this steady state agrees with the one found by VZ. In the second of these examples we repeated the integration for parameter values for which the method of VZ does not converge. The steady state thus obtained has a much more pronounced boundary layer in the north-west of the basin which compares well with the general structure of the solutions obtained numerically by Harrison and Stalos [4] for a square basin.

The last two examples concern an f-plane. In these cases the planetary vorticity is constant. In fact, as a constant value of f does not play a role in the dynamics of (1), it is taken to be zero. The vorticity forcing and Ekman friction are also put to zero, but instead there is a viscosity term $\nu\nabla^2\zeta$ on the right-hand side of (1) and the boundary moves with a prescribed velocity field u_b. Because of the presence of viscosity the no-slip boundary condition is implemented in the way described in Subsection 2.4 of Part I. The first system that we actually consider has a boundary that rotates with an angular velocity ω_b except for a fraction σ that remains stationary due to a fixed sleeve. In the second system that we study the boundary moves with the velocity $\omega_b(1 - \sin\theta)$. Batchelor [2] has shown that, in the limit of vanishing viscosity, the vorticity gets homogenized over regions bounded by closed streamlines. To obtain the actual value of the homogenous vorticity one must consider the flow in boundary layers and for these particular examples these values are $2(1 - \sigma)^{1/2}\omega_b$ and $2(3/2)^{1/2}\omega_b$, respectively, as can be deduced from a general expression obtained by Wood [16]. We discuss the result of two time integrations of 500 time units for the case in which ν is 1/1000 and 1/1024, with the model in $T42$ truncation and—in the first case—a smoothed approximation of the boundary velocity field. We start from vorticity fields that satisfy the boundary condition by giving the coefficients $\zeta_{m|m|}$ the values of (16) and making the other coefficients zero. The integrations indeed result in vorticity fields that are much more homogeneous than the initial states, with vorticity gradients concentrated in relatively narrow layers at the boundary. The last of the two examples comes very close to one of the cases studied by Kuwahara and Imai [6], who used a finite-difference discretization and a relaxation method to obtain steady states of the same system as ours. The cross section of the vorticity along the y-axis, displayed in Fig. 15a, is visually indistinguishable from the cross section in Fig. 3b of Kuwahara and Imai [6].

APPENDIX

Spectral Coefficients of a Rotating Multipole

In this Appendix we will calculate the expansion coefficients of the factor $J_l(\alpha r)\cos l(\theta - \omega t - \mu)$ in the streamfunction and absolute vorticity of the rotating multipole discussed in Subsection 2.1. First, we write

$$J_l(\alpha r)\cos l(\theta - \omega t - \mu) \tag{A1}$$
$$= \tfrac{1}{2}e^{-il(\omega t+\mu)}J_l(\alpha r)e^{il\theta} + \tfrac{1}{2}e^{il(\omega t+\mu)}J_l(\alpha r)e^{-il\theta},$$

from which we see that this term only projects on Y_{ln} and Y_{-ln}. In the following we will show that

$$J_l(\alpha r) = \left(\frac{2}{\alpha}\right) \sum_{k=0}^{\infty} (-1)^k (n+1) J_{n+1}(\alpha) W_{ln}(r), \quad \text{(A2)}$$

where, as we recall, $n = l + 2k$. This means that we have

$$\begin{aligned} &J_l(\alpha r) \cos l(\theta - \omega t - \mu) \\ &\quad = \sum_{n=l}^{\infty} (c_{ln} Y_{ln}(r, \theta) + c_{ln}^* Y_{-ln}(r, \theta)), \end{aligned} \quad \text{(A3)}$$

with

$$c_{ln} = \frac{1}{\alpha} e^{-il(\omega t + \mu)} (-1)^k (n+1) J_{n+1}(\alpha). \quad \text{(A4)}$$

Our starting point in the proof of (A2) is expression (9.1.10) in Abramowitz and Stegun [1]. After substituting $z = \alpha r$ and $\nu = l$, and using that $\Gamma(l + k + 1) = (l + k)!$, this expression reads

$$J_l(\alpha r) = \left(\frac{\alpha r}{2}\right)^l \sum_{k=0}^{\infty} \frac{(-1)^k}{k!(l+k)!} \left(\frac{\alpha r}{2}\right)^{2k}. \quad \text{(A5)}$$

Using the definition of $V_{ln}(r)$ in (5) this can be written as

$$J_l(\alpha r) = \left(\frac{\alpha}{2}\right)^l \sum_{k=0}^{\infty} \frac{(-1)^k}{k!(l+k)!} \left(\frac{\alpha}{2}\right)^{2k} V_{ln}(r). \quad \text{(A6)}$$

It follows from (A21) of Part I that

$$V_{ln}(r) = \sum_{k'=0}^{k} \frac{(l+1+2k')}{(l+1+k+k')} \frac{(k-k'+1)_{k'}}{(l+1+k)_{k'}} W_{ln'}, \quad \text{(A7)}$$

so that

$$\begin{aligned} J_l(\alpha r) = &\left(\frac{\alpha}{2}\right)^l \sum_{k'=0}^{\infty} \sum_{k=k'}^{\infty} \frac{(-1)^k}{k!(l+k)!} \left(\frac{\alpha}{2}\right)^{2k} \\ &\times \frac{(l+1+2k')}{(l+1+k+k')} \frac{(k-k'+1)_{k'}}{(l+1+k)_{k'}} W_{ln'}, \end{aligned} \quad \text{(A8)}$$

where we have changed the order of summations over k and k'. The expression can be simplified by noting that

$$(k-k'+1)_{k'} = (k-k'+1) \cdots k = \frac{k!}{(k-k')!}, \quad \text{(A9)}$$

$$(l+1+k)_{k'} = (l+1+k) \cdots (l+k+k'). \quad \text{(A10)}$$

The latter identity leads to

$$\begin{aligned} &(l+1+k+k')(l+1+k)_{k'} \\ &\quad = (l+1+k) \cdots (l+1+k+k') \\ &\quad = \frac{(l+1+k+k')!}{(l+k)!}. \end{aligned} \quad \text{(A11)}$$

Substituting this in (A8) gives

$$\begin{aligned} J_l(\alpha r) = &\left(\frac{\alpha}{2}\right)^l \sum_{k'=0}^{\infty} (l+1+2k') W_{ln'} \\ &\times \left[\sum_{k=k'}^{\infty} (-1)^k \left(\frac{\alpha}{2}\right)^{2k} \frac{1}{(k-k')!(l+1+k+k')!} \right]. \end{aligned} \quad \text{(A12)}$$

Defining $p = k - k'$, the summation between square brackets becomes

$$\sum_{p=0}^{\infty} (-1)^{p+k'} \left(\frac{\alpha}{2}\right)^{2p+2k'} \frac{1}{p!(l+1+p+2k')!} \quad \text{(A13)}$$

as a result of which

$$\begin{aligned} J_l(\alpha r) = &\left(\frac{2}{\alpha}\right) \sum_{k'=0}^{\infty} (-1)^{k'} (l+1+2k') W_{ln'} \\ &\times \left[\left(\frac{\alpha}{2}\right)^{l+1+2k'} \sum_{p=0}^{\infty} (-1)^p \left(\frac{\alpha}{2}\right)^{2p} \frac{1}{p!(l+1+2k'+p)!} \right]. \end{aligned} \quad \text{(A14)}$$

From (A5) we deduce that the expression between square brackets equals $J_{l+1+2k'}(\alpha)$, so that

$$J_l(\alpha r) = \left(\frac{2}{\alpha}\right) \sum_{k'=0}^{\infty} (-1)^{k'} (l+1+2k') J_{l+1+2k'}(\alpha) W_{ln'}(r). \quad \text{(A15)}$$

Changing from primed to unprimed variables and again using that $n = l + 2k$, we see that this result is identical to (A2).

ACKNOWLEDGMENTS

I thank Dr. H. Clercx for reading the first draft of the manuscript. Drs. R. Pasmanter and H. Brands are thanked for inspiring me to go beyond the free-slip boundary condition. I am grateful to the reviewers for their constructive criticism.

REFERENCES

1. M. Abramowitz and I. A. Stegun, *Handbook of Mathematical Functions* (Dover, New York, 1965).
2. G. K. Batchelor, *J. Fluid Mech.* **1,** 177 (1956).
3. G. K. Batchelor, *An Introduction to Fluid Dynamics* (Cambridge Univ. Press, Cambridge, UK, 1967).
4. D. E. Harrison and J. Stalos, *J. Mar. Res.* **40,** 773 (1982).
5. W. Horton and A. Hasegawa, *Chaos* **4,** 227 (1994).
6. K. Kuwahara and I. Imai, *Phys. Fluids Suppl. II* **12,** 94 (1969).
7. B. Machenhauer, *Numerical Methods Used in Atmospheric Models, Vol. II,* WMO/GARP Publ. Ser. 17, 121 (1979).
8. D. Nof, *Geophys. Astrophys. Fluid Dyn.* **52,** 71 (1990).
9. S. A. Orszag, *J. Atmos. Sci.* **27,** 890 (1970).
10. J. Pedlosky, *Geophysical Fluid Dynamics,* 2nd ed. (Springer-Verlag, New York, 1987).
11. W. H. Press, S. A. Teukolsky, W. T. Vetterling, and B. P. Flannery, *Numerical Recipes in FORTRAN,* 2nd ed. (Cambridge Univ. Press, Cambridge, UK, 1992).
12. P. B. Rhines and W. R. Young, *J. Fluid Mech.* **122,** 347 (1982).
13. C.-G. Rossby, *J. Mar. Res.* **2,** 38 (1939).
14. W. T. M. Verkley, *J. Atmos.* **47,** 2453 (1990).
15. W. T. M. Verkley and J. T. F. Zimmerman, *J. Fluid Mech.* **295,** 61 (1995).
16. W. W. Wood, *J. Fluid Mech.* **2,** 77 (1957).
17. W. T. M. Verkley, *J. Comput. Phys.* **136,** 100–114 (1997).